This is the peer-reviewed, final accepted version for American Mineralogist, published by the Mineralogical Society of America.
The published version is subject to change. Cite as Authors (Year) Title. American Mineralogist, in press.
DOI: https://doi.org/10.2138/am-2023-9138. http://www.minsocam.org/

REVISION 1

THE EFFECT OF *A*-SITE CATIONS ON CHARGE-CARRIER MOBILITY IN FE-RICH AMPHIBOLES

SIMONE BERNARDINI[1,2*], GIANCARLO DELLA VENTURA[2,3,4], JOCHEN SCHLÜTER[5], FRANK. C. HAWTHORNE[6] AND BORIANA MIHAILOVA[1*]

[1]Fachbereich Erdsystemwissenschaften, Universität Hamburg, Grindelallee 48, D-20146 Hamburg, Germany

[2]Dipartimento di Scienze, Università di Roma Tre, Largo S. Leonardo Murialdo 1, 00146 Rome, Italy

[3]INFN-LNF, Via E. Fermi 40, Frascati 00044, Rome, Italy.

[4]INGV, Via di Vigna Murata 605, 00143 Rome, Italy

[5]Mineralogisches Museum, Leibniz-Institut zur Analyse des Biodiversitätswandels, Grindelallee 48, D-20146 Hamburg, Germany

[6]Department of Earth Sciences, University of Manitoba, Winnipeg, Manitoba R3T 2N2, Canada

Corresponding authors: **SB:** simone.bernardini@uniroma3.it; simone.bernardini@uni-hamburg.de; **BM:** boriana.mihailova@uni-hamburg.de

ABSTRACT

Elucidating the high-temperature behavior of rock-forming minerals such as amphiboles ($AB_2C_5T_8O_{22}W_2$) is critical for the understanding of large-scale geological processes in the lithosphere and in particular the development of high conductivity in the Earth's interior. Recently, we have shown that at elevated temperatures, ^{C}Fe-bearing amphiboles with a vacant *A* site develop two types of charge carrier: (1) small polarons, and (2) delocalized H^+ ions.

To elucidate the effect of *A*-site cations on the formation and stability of charge carriers within the amphibole structure, here we analysed synthetic potassic-ferro-richterite

as a model Fe-rich amphibole with a fully occupied *A* site *via in situ* temperature-dependent Raman spectroscopy. We further compare the results from *in situ* time-dependent Raman-scattering experiments on pre-heated and rapidly quenched potassic-ferro-richterite and riebeckite, as a model Fe-rich amphibole with a vacant *A* site.

We show that the presence of *A*-site cations: (1) reduces the activation temperature of mobile polarons and delocalized H^+ cations; (2) decreases the magnitude of the polaron dipole moment; (3) slows down the process of re-localization of electrons on cooling; (4) makes the electrons inert to rapid change in external conditions, supporting the persistence of a metastable state of pre-activated delocalized electrons even at room temperature.

Our results have important implications in Earth Sciences demonstrating that the *A*-site cations may control the depth of development of high-conductivity in subducted amphibole-bearing rocks. Moreover, from the view point of mineral-inspired materials science, our results suggest that the amphibole-structure type has great potential for designing functional materials with tuneable anisotropic-conductivity properties.

Keywords: iron-rich amphiboles, riebeckite, synthetic potassic-ferro-richterite, *in situ* high-temperature Raman spectroscopy, polaron conductivity, hydrogen diffusion

1. INTRODUCTION

Amphibole-group minerals are important constituents in igneous and metamorphic rocks, being stable over a wide range of temperature and pressure. They have unusually high chemical variability, accommodating a wide range of elements in their structure (*e.g.,* Hawthorne and Oberti, 2007). The general formula of the amphiboles is written as $AB_2C_5T_8O_{22}W_2$, where A = Na, K, □ (vacancy) at the *A*(2) and *A*(*m*) sites, B = Na, Ca, Li, Mg, Fe^{2+}, Mn^{2+} at the *M*(4) site, C = Mg, Fe^{2+}, Fe^{3+} Mn^{2+}, Al, Ti, Cr, V at the *M*(1,2,3) sites, T = Si, Al, Ti at the *T*(1,2) sites and W = OH, F, Cl, O^{2-} at the *W* site (Hawthorne et al. 2012). The structure consists of ribbons of six-membered rings of TO_4 tetrahedra linked to ribbons of MO_6 octahedra, forming I-beams that extend along the **c** axis (Fig. 1a). The I-beams are arranged in a zig-zag fashion in the (**a***,**b**) plane (Fig. 1b) and the B cations link the I-beams into a three-dimensional structure.

The ability of amphiboles to retain their structure when their constituent Fe^{2+} oxidizes to Fe^{3+} with increasing temperature depends on local bonding between octahedrally coordinated Fe^{2+} and $(OH)^-$ (Fig. 1a). In the presence of external oxygen, Fe^{2+} turns into Fe^{3+} following the reaction: $2Fe^{2+} + 2^{W}(OH)^- + 0.5^{ex}O_2 \rightarrow 2Fe^{3+} + 2e^- + 2^{W}O^{2-} + 2H^+ + 0.5^{ex}O_2 \rightarrow 2Fe^{3+} + 2^{W}O^{2-} + {}^{ex}H_2O$ (Della Ventura et al. 2018a; Mihailova et al. 2022, Bernardini et al. 2023), where the local charge imbalance due to Fe oxidation is compensated by the delocalization of H^+ and e^- in the crystal bulk, before their loss in the surroundings. Because of this process, an Fe-bearing amphibole may transform into an oxo-amphibole, thus enlarging significantly its stability field up to very high temperature (Oberti et al. 2018, Della Ventura et al. 2023a). An important implication of the above reaction is that Fe-amphiboles may develop two types of charge carrier with increasing temperature: (1) small polarons, and (2) delocalized H^+ (Mihailova et al. 2021, 2022; Rösche et al. 2022; Bernardini et al. 2023). Small polarons result from electrons excited between hybridized 2*p* levels of oxygen and 3*d* levels of octahedrally coordinated Fe^{2+} (Mihailova et al. 2021) that couple with longitudinal optical (LO) polar FeO_6 phonons to carry the associated local structural distortion across the crystal bulk (Fig. 2). The structural flexibility of the silicate rings allows them to connect to neighbouring octahedra of variable size *via* slight tilting and rotation of the tetrahedra, a feature that is critical to the development of hopping polarons (Mihailova et al. 2021; 2022; Bernardini et al. 2023).

Details of the atomistic mechanisms involved in the development of small polarons and mobile H^+ during redox processes in amphiboles are of paramount interest in a range of disciplines, including geophysics and materials science, because (i) amphiboles are important constituents of subduction-zone rocks with anomalously high electrical conductivity (Ichiki et al. 2009; Kasaya et al. 2005), and (ii) synthetic amphibole counterparts can be the basis for designing functional materials with anisotropic polaron conductivity at high temperatures.

In inelastic light-scattering experiments, the interaction between the electron and the phonon with the incoming photon during the activation of polarons gives rise to resonance Raman scattering (RRS) (Mihailova et al. 2021). Resonance conditions are achieved when valence electrons are excited to the conduction band and interact with longitudinal optical (LO) polar phonons *via* the so called Fröhlich interactions, *i.e.*,

This is the peer-reviewed, final accepted version for American Mineralogist, published by the Mineralogical Society of America.
The published version is subject to change. Cite as Authors (Year) Title. American Mineralogist, in press.
DOI: https://doi.org/10.2138/am-2023-9138. http://www.minsocam.org/

electrostatic interactions between the conduction electron and the dipole moment induced by a polar atomic vibration (Yu and Cardona, 2010). As a result of the electron-phonon coupling, under resonance conditions the symmetry selection rules are modified and the polar optical modes related to the atomic species in which the electron transition occurs are enhanced (de la Flor et al., 2014). In centrosymmetric crystals like amphiboles, this leads to selective enhancement of those polar phonon modes (initially Raman-inactive) related to the atomic species in which the electron transition occurs (*i.e.,* FeO_6 octahedra in the amphibole structure, see Fig 2a), and suppression of all other Raman-active modes (*i.e.*, the OH-stretching and silicon-oxygen vibrations, Mihailova et al. 2021; 2022; Rösche et al. 2022; Bernardini et al. 2023). The temperature of polaron activation in the structure depends on the sample composition; our previous Raman studies on amphiboles with a vacant *A* site showed that the presence of $^{C}Fe^{3+}$ reduces the temperatures of onset (T') and completion (T'') of electron delocalization, whereas ^{C}Mg shifts them toward higher temperatures (Mihailova et al. 2021; 2022; Rösche et al. 2022; Bernardini et al. 2023).

In this paper, we present the results of Raman-scattering analysis of synthetic potassic-ferro-richterite (PFR), nominally $^{A}K^{B}(CaNa)^{C}Fe^{2+}{}_{5}{}^{T}Si_8O_{22}(OH)_2$, as a representative Fe-rich amphibole with a filled *A* site. The intent of this study is to address the effect of ^{A}K on the thermal activation of charge carriers under both reducing and oxidizing conditions. The resultant data will be compared to the data obtained for riebeckite (RB), nominally $^{A}\square^{B}Na_2{}^{C}(Fe^{2+}{}_3Fe^{3+}{}_2)^{T}Si_8O_{22}(OH)_2$ (Bernardini et al. 2023), as a proxy for a vacant *A*-site amphibole. Additional time-dependent experiments on both PFR and RB were aimed at constraining the kinetics of e^- and H^+ re-localization upon fast cooling in an inert (N_2) atmosphere in structures with empty *vs.* filled *A* sites.

2. MATERIALS AND METHODS

In this work, we examine a synthetic PFR (Redhammer and Roth 2002; Oberti et al. 2016) and a near-end-member RB from an alkali pegmatite, Mt. Malosa, Zomba District, Malawi (Susta et al. 2018; Oberti et al. 2018). Both amphiboles have monoclinic *C*2/*m* symmetry at ambient conditions and their crystal-chemical formulae have been derived via a full spectrum of analytical techniques (for details see the above references). The actual chemical composition of PFR is

This is the peer-reviewed, final accepted version for American Mineralogist, published by the Mineralogical Society of America.
The published version is subject to change. Cite as Authors (Year) Title. American Mineralogist, in press.
DOI: https://doi.org/10.2138/am-2023-9138. http://www.minsocam.org/

$^{A}(K_{0.90}Na_{0.07}\square_{0.03})^{B}(Ca_{0.54}Na_{1.46})^{C}(Fe^{2+}{}_{4.71}Fe^{3+}{}_{0.79})^{T}Si_{8}O_{22}{}^{W}[(OH)_{1.70}O_{0.30}]$,

while that of RB is

$^{A}(\square_{0.9}K_{0.06}Na_{0.04})^{B}(Na_{1.82}Ca_{0.13}Fe^{2+}{}_{0.05})^{C}(Fe^{2+}{}_{2.94}Fe^{3+}{}_{1.64}Mg_{0.26}Al_{0.10}Mn^{2+}{}_{0.05}Ti_{0.01})$

$^{T}(Si_{7.9}Al_{0.03})O_{22}{}^{W}[(OH)_{1.90}F_{0.10}]$

The Raman spectra were collected with a Horiba Jobin-Yvon T64000 triple-monochromator spectrometer equipped with an Olympus BX41 microscope and a liquid-N_2-cooled charge-couple-device detector, using the 514.532-nm line of a Coherent Innova 90 C FreD Ar^+ laser. The spectrometer was calibrated to the Raman peak of Si at 520.5 cm^{-1}. The spectral resolution was ~2 cm^{-1} and the instrumental precision in determining the peak positions was ~0.35 cm^{-1}.

In situ temperature-dependent experiments on PFR were done in N_2 with a LINKAM THMS-E600 and in air with a LINKAM TS1200 EV-1015, with temperature accuracies of 0.1 K and 1 K, respectively. Pristine euhedral crystals of similar size (~50 × 50 × 200 μm^3) were used for each run. Parallel polarized spectra (polarization of the scattered light $\mathbf{E}_s$ parallel to the polarization of the incident light $\mathbf{E}_i$) were collected in backscattering geometry in two different orientations: **c** axis || $\mathbf{E}_i$ and **c** axis ⊥ $\mathbf{E}_i$, which correspond to $\bar{y}(zz)y$ and $\bar{y}(xx)y$ in Porto's notation, with z along the **c** axis and $x \perp y \perp z$ (Mihailova et al. 2021). Both types of polarized Raman spectra are dominated by A_g phonon modes, but different components of the Raman polarizability tensor are detected in the two scattering geometries, indicating orientational dependence of Raman intensities also under non-resonance conditions (Waeselmann et al. 2020, Mihailova et al. 2021). A complete group-theory analysis of the amphibole phonon modes is given by Waeselmann et al. (2020).

Temperature-dependent experiments were conducted in the 300 - 600 K range, because this interval was sufficient to observe the development of charge carriers. A heating/cooling rate of 10 K/min was used for the experiments in N_2, whereas in air the heating rate was 20 K/min and the cooling rate was 50 K/min. The sample was stabilized 5 min at each target T before collecting the spectrum. Temperature values for each ramp, scattering geometry, and different atmosphere are given in Table 1.

In addition, *in situ* time-dependent experiments were done on PFR and RB with the **c** axis || $\mathbf{E}_i$ in an N_2 atmosphere at 300 K after heating the sample at a rate of 10 K/min up

This is the peer-reviewed, final accepted version for American Mineralogist, published by the Mineralogical Society of America.
The published version is subject to change. Cite as Authors (Year) Title. American Mineralogist, in press.
DOI: https://doi.org/10.2138/am-2023-9138. http://www.minsocam.org/

to T'' (*i.e.,* temperature of complete activation of polaron: 525 and 650 K for PFR and RB, respectively) and kept at this temperature for 30 min before cooling at a rate of 50 K/min. Purging with N_2 was used to avoid the ejection of charge carriers from the crystal surface (Mihailova et al. 2021; Bernardini et al. 2023) thus allowing to monitor their re-localization on cooling. Raman spectra were collected immediately when the samples reached 300 K, and the measurements were repeated every 15 minutes until no further spectral changes were visible, *i.e.*, 150 min for RB and 240 min for PFR.

The measured spectra were baseline-corrected, temperature-reduced for the Bose-Einstein population factor, and fitted with pseudo-Voigt functions to derive the phonon wavenumbers ω, full widths at a half maximum (FWHM), integrated intensities I, and weight coefficients q of the Lorentzian contribution to the peak shape. Details of the data-evaluation procedure are given in the supplementary material of Mihailova et al. (2021).

3. RESULTS

3.1. *In situ* HT experiments on potassic-ferro-richterite

In situ temperature-dependent Raman spectra collected in air with $\mathbf{E}_i \parallel \mathbf{c}$ show that the OH-stretching mode disappears at 500 K (Fig. S1) while the overall scattering changes drastically at 520 K: the MO_6 and the silicate phonon modes are completely suppressed and a strong peak due to RRS appears near 570 cm^{-1} (red spectrum in Figs. 3a and S1). However, the Raman spectra collected with $\mathbf{E}_i \perp \mathbf{c}$ at the same temperature still follow the conventional selection rules (red spectrum in Figs. 3b and S2). This clearly demonstrates the development of mobile polarons with electric dipoles aligned parallel to the **c** axis, as already shown to occur for grunerite (GR), nominally $^{A}\square^{B}Fe_2{}^{C}Fe^{2+}{}_5{}^{T}Si_8O_{22}(OH)_2$, and RB (Mihailova et al. 2021; Bernardini et al. 2023). The temperature evolution of the wavenumber of the SiO_4-ring mode $\omega_{671\ \mathrm{cm}^{-1}}^{\mathrm{ring\ mode}}(\mathrm{T})$ near 671 cm^{-1} is sensitive to the local structural readjustment within the silicate double-chains. The $\omega_{671\ \mathrm{cm}^{-1}}^{\mathrm{ring\ mode}}(\mathrm{T})$ trend derived from the $\mathbf{E}_i \parallel \mathbf{c}$ spectra (red spheres in Figure 4a) shows a minimum at T' = 460 K, whereas that derived from the $\mathbf{E}_i \perp \mathbf{c}$ spectra (green rhombuses in Fig. 4a) shows a minimum at higher temperature, T'' = 525 K, where RRS becomes dominant in $\mathbf{E}_i \parallel \mathbf{c}$ geometry. After cooling from 540 K in $\mathbf{E}_i \parallel \mathbf{c}$ and from 600 K in $\mathbf{E}_i \perp \mathbf{c}$ geometry, the $\omega_{671\ \mathrm{cm}^{-1}}^{\mathrm{ring\ mode}}$ (Fig. 4a)

approaches a higher value that the initial one, indicating irreversible modification of the ring geometry due to permanent Fe oxidation (Mihailova et al. 2021; Bernardini et al. 2023). Irreversible $^{M}Fe^{2+} \rightarrow {}^{M}Fe^{3+}$ and $^{W}(OH)^{-} \rightarrow {}^{W}O^{2-}$ changes are also confirmed by the disappearance of the peak near 197 cm^{-1} (see Fig. 4b), related to a Raman-active $^{M}Fe^{2+}O_6$ phonon mode (Susta et al. 2018), and the OH-stretching mode, near 3675 cm^{-1} (see Figs. 5a and 5b). Hence, dehydrogenation in air is completed in the temperature range 540-600 K, which is in accord with the temperature at which changes in the unit-cell parameters occur due to the irreversible oxidation (Oberti et al. 2016).

In situ $\mathbf{E}_i \parallel c$ spectra collected in an N_2 atmosphere show that RRS is dominant at 500 K (red spectrum in Figs. 3c and S3). However, at this temperature, the $\mathbf{E}_i \perp \mathbf{c}$ spectrum still exhibits the phonon modes related to silicate anion and the MO_6 octahedra, although the OH-stretching is no longer resolved (red spectrum in Figs. 3d and S4). This demonstrates the development of anisotropic mobile polarons also in N_2 atmosphere. The $\mathbf{E}_i \parallel c$ spectra collected immediately after quenching are still dominated by RRS (Fig. S3) while the $\mathbf{E}_i \perp \mathbf{c}$ spectrum shows no detectable recovery of the OH-stretching mode once reaching 300 K (Fig. S4). However, the spectra collected (in both scattering geometries) after prolonged time (t ~ 120 min) show total recovery of all non-RRS peaks (*i.e.,* the phonon modes related to silicate anion, the MO_6 octahedra, and the hydroxyl groups, see Figs. 3c, 3d, S3, and S4). Similarly to the experiments in air, the $\omega_{671\ \mathrm{cm}^{-1}}^{\mathrm{ring\ mode}}(T)$ derived from the $\mathbf{E}_i \parallel \mathbf{c}$ spectra show a clear minimum at 450 K (red spheres in Fig. 4c). However, after cooling to room temperature and a certain waiting time (~ 120 min) after the heating-cooling ramp, the SiO_4 mode shifts back to 671 cm^{-1} (blue spheres in Fig. 4c), indicating a reversible temperature-induced modification of the silicate double-chain geometry. The recovery of $I_{n\ 197}^{\mathrm{MO_6}}$ and $I^{\text{OH stretching}}/I^{\text{framework}}$ at room temperature and waiting for ~120 min after cooling to room temperature (Figs. 4d, 5c, and 5d) also confirms that reversible $^{M}Fe^{2+} \leftrightarrow {}^{M}Fe^{3+}$ and $^{W}(OH)^{-} \leftrightarrow {}^{W}O^{2-}$ exchange takes place. Note that the small quantitative difference between $I_{n\ 197}^{\mathrm{MO_6}}$ measured before and after the heating-cooling ramp is most probably due to insufficient waiting time (see the discussion below), but the trend towards a complete disappearance of RRS and full recovery of non-RRS signals is clear.

This is the peer-reviewed, final accepted version for American Mineralogist, published by the Mineralogical Society of America.
The published version is subject to change. Cite as Authors (Year) Title. American Mineralogist, in press.
DOI: https://doi.org/10.2138/am-2023-9138. http://www.minsocam.org/

3.2. Time-dependent experiments at RT on riebeckite and potassic-ferro-richterite annealed in N_2

To address the re-arrangement of e^- and H^+ upon cooling, we did time-dependent experiments on both PFR and RB in N_2, to avoid loss of e^- and H^+ that occurs in amphiboles when heated in an oxidizing atmosphere (Bernardini et al. 2023 and this work).

As described in the experimental section, RB and PFR single crystals oriented in $\mathbf{E}_i \parallel \mathbf{c}$ scattering geometry were heated at a rate of 10 K/min to 650 K and 525 K (T" in Table 2), respectively, and held at these two temperatures for 30 min to achieve collective e^- delocalization, revealed *via* the appearance of RRS (red spectra in Fig. 6). Then the samples were quenched at a relatively high cooling rate (50 K/min) and Raman spectra were collected immediately, without any stabilization time, and the measurements were repeated every 15 minutes to monitor the relaxation of the electronic system as a function of time.

The spectrum of RB collected immediately after fast cooling (t_0) completely recovers its initial non-RRS peaks (blue spectrum in Fig. 6a). In strong contrast, the spectrum of PFR collected at t_0 is still dominated by RRS and only weak non-RRS peaks are resolved (blue spectrum in Fig. 6b). However, the RRS signals fully reappear after 15 min and 30 min for RB and PFR, respectively (green spectra in Fig. 6), showing that electron delocalization re-occurs at room temperature. The OH-stretching peak also disappears, but this can be due to the change in the selection rules, not due to further delocalization of H^+ at RT. For RB, all non-RRS peaks, including the OH-stretching peak, reappear abruptly after 90 min (orange spectrum in Fig. 6a), and after 135 min, total recovery of the conventional (non-resonant) Raman spectrum is observed (grey spectrum in Fig. 6a), without any further change with time. For PFR, the non-RRS peaks start reappearing after 135 min (orange spectrum in Fig. 6b) and their intensities gradually increase while those of RRS signals vanish until complete recovery of the non-RRS spectrum after 240 min (grey spectrum in Fig. 6b). These observations indicate that the presence of *A*-site cations delays the relaxation of the system from a metastable state with conductive electrons to the ground state with all electrons re-localized back to $^{M}Fe^{2+}$ cations.

This is the peer-reviewed, final accepted version for American Mineralogist, published by the Mineralogical Society of America.
The published version is subject to change. Cite as Authors (Year) Title. American Mineralogist, in press.
DOI: https://doi.org/10.2138/am-2023-9138. http://www.minsocam.org/

The electron relaxation can be quantitatively monitored by the time evolution of the fractional intensity of the $^{M}Fe^{2+}O_6$ mode near 197 cm^{-1} normalized to the corresponding intensity measured before heating the sample ($I^{MO_6}_{n(t)}/I^{MO_6}_{n(NA)}$), and by the intensity ratio between the SiO_4-ring mode near 660 cm^{-1} and the strongest RRS peak near 580 cm^{-1} ($I^{ring\ mode}/(I^{ring\ mode}+I^{RRS})$). Data for RB and PFR are compared in Figs. 7a and 7b. Immediately after cooling (t_0 = 0 min), RB (orange spheres) shows rapid and almost complete re-localization of e^- ($I^{MO_6}_{n(t)}/I^{MO_6}_{n(NA)}$ and $I^{ring\ mode}/(I^{ring\ mode}+I^{RRS}) \sim 0.8$). In contrast, PFR (green spheres) shows sluggish and only partial re-localization of e^- ($I^{MO_6}_{n(t)}/I^{MO_6}_{n(NA)}$ and $I^{ring\ mode}/(I^{ring\ mode}+I^{RRS}) \sim 0.2$). Electron delocalization still occurs at room temperature in RB and PFR after 15 and 30 min, respectively ($I^{MO_6}_{n(t)}/I^{MO_6}_{n(NA)}$ and $I^{ring\ mode}/(I^{ring\ mode}+I^{RRS}) \sim 0$). This state of collectively delocalized e^- persists at room temperature up to 75 min in RB and 120 min in PFR. It is worth noting that in RB, partial re-localization of e^- occurs at 45 min, as shown by $I^{MO_6}_{n(t)}/I^{MO_6}_{n(NA)} \sim 0.2$ (see Fig. 7a). Finally, renewed electron re-localization starts after 90 min and it is completed after 135 min in RB. For PFR this process is much slower, starting only after 135 min and ending up after 240 min in PFR (*i.e.*, $I^{MO_6}_{n(t)}/I^{MO_6}_{n(NA)}$ and $I^{ring\ mode}/(I^{ring\ mode}+I^{RRS}) \sim 1$).

4. DISCUSSION

4.1. Temperature-activated charge carriers in potassic-ferro-richterite

The appearance of direction-dependent RRS at elevated temperatures (see the spectra collected in $\mathbf{E}_i \parallel \mathbf{c}$ *vs.* $\mathbf{E}_i \perp \mathbf{c}$ scattering geometry in Fig. 3) clearly shows that the formation of strongly anisotropic small polarons with dipoles parallel to the **c** axis occurs also in PFR. Similar to grunerite (Mihailova et al. 2021) and riebeckite (Bernardini et al. 2023), in a reducing atmosphere the process of e^- and H^+ delocalization is fully reversible, emphasising that mobile charge carriers are typical of Fe-bearing amphiboles at elevated temperature, regardless of the degree of *A*-site occupancy and presence of external oxygen. The activation of small polarons requires a readjustment of the SiO_4 ring-geometry to adapt to the smaller size of the $Fe^{3+}O_6$ octahedra compared to that of $Fe^{2+}O_6$ (*e.g.*, Mihailova et al. 2022). Following the concept of hard-mode spectroscopy (Bismayer 1990), this local-

This is the peer-reviewed, final accepted version for American Mineralogist, published by the Mineralogical Society of America.
The published version is subject to change. Cite as Authors (Year) Title. American Mineralogist, in press.
DOI: https://doi.org/10.2138/am-2023-9138. http://www.minsocam.org/

scale structural change can be experimentally detected by a minimum in $\omega^{\text{ring mode}}$(T). As already observed for riebeckite (Bernardini et al. 2023) and grunerite (Mihailova et al. 2021; 2022), the $\omega^{\text{ring mode}}$(T) trends derived from the different scattering geometries show minima at different temperatures, which in the case of PFR are T' = 460 K for $\mathbf{E}_i \parallel \mathbf{c}$ and T'' = 525 K for $\mathbf{E}_i \perp \mathbf{c}$ (Fig. 4a). The difference between T' and T'' reveals that the temperature-induced flattening of the energy potential U related to SiO_4-ring readjustment is faster along the SiO_4-MO_6 stripes than in the perpendicular direction. This is because the development of polarons with mutually aligned electrical dipoles along the **c** axis gives rise to an intrinsic electric field || **c** and consequently, to an additional potential vector term $\boldsymbol{\delta U} \propto$ T''-T' (Mihailova et al. 2022; Bernardini et al. 2023). For PFR T''-T' = ~65 K, which corresponds to ~0.0056 eV. Thus, T' = 460 K pinpoints the onset of formation of polarons in PFR, whereas T'' = 525 K, which is also the temperature at which anisotropic RRS occurs, marks the development of collective mobile polarons. In an oxidizing atmosphere the delocalization of H^+ is strongly enhanced above T'' (see Fig. 5b) and after reaching 600 K the OH-stretching peak does not recover even partially on subsequent cooling down. That is, near 600 K the irreversible $^{M}Fe^{2+} + {}^{W}(OH)^{-} \rightarrow {}^{M}Fe^{3+} + {}^{W}O^{2-}$ co-exchange is complete and PFR becomes an oxo-amphibole. Given that the temperature step in our experiment was 25 K, this value is consistent with the oxidation temperature deduced from X-ray absorption spectroscopy (588 K) and X-ray diffraction (608 K) (Della Ventura et al. 2018b) for the same sample.

4.2. Thermally-activated charge carriers in amphiboles: occupied *A* site *versus* vacant *A* site

Table 2 compares the characteristic temperatures T' and T'' for PFR (this study), GR (Mihailova et al. 2021) and RB (Bernardini et al. 2023). As can be seen, the presence of *A*-site cations reduces both T' and T'', indicative of potential barrier for polaron activation, as well as the temperature difference T''-T', indicative of the polaron-dipole magnitude. This can be due to the smaller energy gap E_g between the valence and conduction electrons bands and/or smaller local structural deformation associated with the polaron occurrence. The former reason can be ruled out, because density-functional-theory (DFT) calculations of the electron structure of nominal PFR (Della Ventura et al. 2018b)

and GR (Mihailova et al. 2021), both having only Fe^{2+} in the octahedral strips, show that E_g is smaller for GR. Therefore, one can speculate that a filled *A* site reduces the degree of local structural deformation, implying weaker electron-phonon interactions and hence, a smaller effective polaron mass as compared to the case of *A*-site vacant amphiboles. However, the mobility of polarons, depends not only on the effective mass but also on the mean free path of charge carriers (*e.g.*, Kittel 2004), which might be reduced in the presence of *A*-site cations due to additional collision processes that hopping polarons may experience.

The *in situ* heating-cooling experiments in N_2 demonstrate another peculiarity of *A*-site filled amphiboles. In strong contrast to RB (Della Ventura et al. 2018a, Bernardini et al. 2023) and GR (Mihailova et al. 2021), the spectra of PFR collected in N_2 do not recover immediately after cooling to room temperature (see Figs. 3, 4, 5, S3, and S4). Only after at least two hours, the non-resonance spectral features fully reappear and RRS entirely disappear. Therefore, once e^- and H^+ are delocalized at elevated temperatures, their corresponding re-localization at the octahedrally coordinated Fe cations and *W*-site anions is slowed by the filled *A* sites. That is, the *A*-site cations act as a "retardant" for immobilizing the charge carriers when the temperature decreases and slow down the transition from the metastable "semi-conductive" state to the ground insulating state of amphibole at room temperature. In other words, for PFR as a model amphibole with occupied *A* sites, the depth of the potential well representing the metastable state is close to that of the primary ground state, making the electrons inert to a rapid change of external conditions. The results of the kinetics experiments in N_2 show that the relaxation of the electronic system occurs faster in a vacant-*A*-site amphibole than in an occupied-*A*-site amphibole (although RB was heated to a higher temperature than PFR, 650 K *versus* 525 K, respectively). However, the time evolution of $I_{n(t)}^{\mathrm{MO}_6}/I_{n(NA)}^{\mathrm{MO}_6}$ and $I^{ring\ mode}/(I^{ring\ mode}+I^{RRS})$ (see Fig. 7) shows fluctuations of the electronic system until complete and stable e^- re-localization is achieved at room temperature, after thermal treatment. As the experimental conditions were isothermal but not adiabatic, the fast cooling down should have led to a significant temperature gradient from the crystal core to the rim and therefore, to a propagation of temperature waves, which in turn causes chemical fluctuations in the surface layer (a few μm thick) probed by Raman spectroscopy, *i.e.*, fluctuation of $Fe^{3+} \leftrightarrow$

This is the peer-reviewed, final accepted version for American Mineralogist, published by the Mineralogical Society of America.
The published version is subject to change. Cite as Authors (Year) Title. American Mineralogist, in press.
DOI: https://doi.org/10.2138/am-2023-9138. http://www.minsocam.org/

Fe^{2+}, corresponding to delocalized and re-localized electrons. Hence, we attribute the observed re-excitation of electrons at room temperature to a temperature wave from the core to the surface of the crystal. In RB, this process happens quickly and abruptly, with strong oscillations of the electronic system, whereas in PFR the relaxation is smooth and sluggish (see Fig. 7). This inference is in agreement with the resistivity measurements done recently by Della Ventura et al. (2023b) showing fast oscillation of conductivity in RB while cycling the sample temperature. The prolonged time of recovery for PFR, independent of the cooling rate, confirms that *A*-site cations enlarge the potential barrier between the metastable state of Fe^{3+} cations with electrons hopping between adjacent MO_6 octahedra and the ground state of octahedrally coordinated Fe^{2+}. This implies that thermally activated polaron conductivity in amphiboles might be some way tuned *via* the *A*-site population.

It is worth noting that the polaron hopping through the I-beams should involve rapidly changing sizes of the MO_6 octahedra. As a result, the strips of *M*(1,2,3) octahedra should develop dynamical modulation in its dimensions as the polaron migrates along the **c**-axis direction. Consequently, the linkage between the *M*(1,2,3) and $[T_8O_{22}]$ strips must also have a complementary modulation in order to maintain this linkage. Hawthorne (1979) examined the details of the linkages in monoclinic amphiboles between the strips of octahedra and tetrahedra. The intrinsic differences between the dimensions of the two strips are accommodated primarily by rotation of the tetrahedra within the (**b**,**c**) plane such that larger cations at the *M*(1,2,3) sites are associated with less TO_4 rotations, *i.e.*, larger O5-O7-O5 and O5-O6-O7 angles (see Fig. 1a) and consequently different TO_4-ring geometry, mirrored by $\omega^{\text{ring mode}}_{\sim 670\ \text{cm}^{-1}}$. The presence of *A*-site cations increases the number of bonds to the bridging oxygen atoms O5, O6, and O7, which would allow them much more flexibility in their movement to accommodate the mobile polarons and maintain their accord with the valence-sum rule (Brown 2016). This greater flexibility can support keeping smaller $^{C}Fe^{3+}$ in the octahedral strips, which effectively stabilizes the state with delocalized electrons at temperatures below the temperature of polaron activation and slows down the kinetics of electron re-localization.

CONCLUSIONS AND IMPLICATIONS

Our *in situ* temperature-dependent Raman data, collected in air or N_2, provide direct proof for the activation of charge carriers in potassic-ferro-richterite as a model Fe-rich amphibole with a completely occupied *A* site. The development of charge carriers begins at T' ~ 460 K, regardless of the presence of external O_2. However, external O_2 is essential for allowing ejection of H^+ and e^- from the crystal surface above T" ~ 525 K. We show that *A*-site cations: (1) reduce the magnitude of the polaron dipole and temperature of polaron activation; (2) slow down the process of re-localization of electrons, and (3) enlarge the potential barrier between the metastable state consisting of effectively $^{M}Fe^{3+}$ and electronic polarons hopping along the MO_6 strips, and the ground state comprising $^{M}Fe^{2+}$, supporting the persistence of a metastable state of delocalized electrons even at room temperature.

Our results thus demonstrate that the *A*-site population can be used to design novel amphibole-inspired functional materials with tuneable anisotropic-conductivity properties, *i.e.*, polaron activation temperature and polaron-dipole magnitude. Moreover, our results have paramount implications for the high-conductivity anomalies observed in subduction zones and the water cycling in the Earth's interior. We show that the *A*-site cations do not prevent the formation of polarons and delocalized H^+ cations, instead they decrease the temperature of activation of charge carriers and dehydrogenation in the amphibole. Although in Fe-poor amphiboles, such as those occurring in the upper-mantle (Konzett et al. 1997; Wilkinson and Le Maitre, 1996, Wagner et al. 1996), the activation of charge carriers and dehydrogenation is expected at much higher temperatures (Rösche et al. 2022; Mihailova et al. 2021; 2022), the presence of *A*-site filled cations in subducting rocks can reduce the activation temperature of charge carries, thus controlling the depth of development of high-conductivity layers in the crust-mantle. The *A*-site population can also control the depth of release of water from amphibole-bearing rocks, with consequences on magmatism and seismicity at convergent plate boundaries.

FUNDING

Deutsche Forschungsgemeinschaft (Project MI 1127/7-2)

MIUR-Italy Dipartimenti di Eccellenza (ARTICOLO 1, COMMI 314-337 LEGGE 232/2016). FCH is supported by a Discovery Grant from the Natural Sciences and Engineering Research Council of Canada.

CONFLICTS OF INTEREST

There are no conflicts to declare

AVAILABILITY OF DATA AND MATERIAL

The data sets generated and analysed during the current study are available from the corresponding authors on reasonable request

AUTHORS' CONTRIBUTIONS

SB collected, evaluated, and analysed the data, and wrote the first draft of the paper. BM, GDV, JS and FCH contributed to data analyses and revised the text.

ACKNOWLEDGEMENTS

Financial support by the Deutsche Forschungsgemeinschaft (MI 1127/7-2) as well as by the Grant to Department of Science, Roma Tre University (MIUR-Italy Dipartimenti di Eccellenza, ARTICOLO 1, COMMI 314-337 LEGGE 232/2016) is gratefully acknowledged. Gunther Redhammer (University of Salzburg) kindly provided the synthetic potassic-ferro-richterite crystals studied here. Thanks are due to G. Iezzi and an anonymous reviewer for positive criticism and suggestions that helped to improve the clarity of the paper.

REFERENCES

Bernardini, S., Della Ventura, G., Schlüter, J., and Mihailova, B. (2023) Thermally activated electron hopping in Fe-rich amphiboles: Implications for the high-conductivity anomalies in subduction zones. Geochemistry, 83, 125942. https://doi.org/10.1016/j.chemer.2022.125942

Bismayer, U. (1990) Hard mode Raman spectroscopy and its application to ferroelastic and ferroelectric phase transitions. Phase Transitions, 27, 211–267. https://doi.org/10.1080/01411599008206910

Brown, I.D. (2016) The chemical bond in inorganic chemistry. The Bond Valence Model. 2nd edition. Oxford University Press, U.K.

de la Flor, G., Wehber, M., Rohrbeck, A., Aroyo, M.I., Bismayer, U., and Mihailova, B. (2014) Resonance Raman scattering of perovskite-type relaxor ferroelectrics under non-ambient conditions. Physical Review B, 90, 064107. https://doi.org/10.1103/PhysRevB.90.064107

Della Ventura, G., Mihailova, B., Susta, U., Cestelli Guidi, M., Marcelli, A., Schlüter, J., and Oberti, R. (2018a) The dynamics of Fe oxidation in riebeckite: a model for amphiboles. American Mineralogist, 103, 1103–1111. https://doi.org/10.2138/am-2018-6382

Della Ventura, G., Galdenzi, F., Cibin, G., Oberti, R., Xu, W., Macis, S., and Marcelli, A. (2018b) Iron oxidation dynamics vs. temperature of synthetic potassic-ferro-richterite: a XANES investigation. Physical Chemistry Chemical Physics, 20, 21764–21771. https://doi.org/10.1039/C8CP04249G

Della Ventura, G., Redhammer, G.J., Galdenzi, F., Ventruti, G., Susta, U., Oberti, R., Radica, F., and Marcelli, A. (2023a) Oxidation or cation re-arrangement? Distinct behaviour of riebeckite at high temperature. American Mineralogist, 108, 59–69. https://doi.org/10.2138/am-2022-8073

Della Ventura, G., Galdenzi, F., Marcelli, A., Cibin, G., Oberti, R., Hawthorne, F.C., Bernardini, S., Mihailova, B. (2023b) *In situ* simultaneous Fe *K*-edge XAS spectroscopy and resistivity measurements of riebeckite: implications for anomalous electrical conductivity in subduction zones. *Geochemistry* https://doi.org/10.1016/j.chemer.2023.126037

Hawthorne, F.C. (1979) The crystal chemistry of the amphiboles. X. Refinement of the crystal structure of ferroglaucophane and an ideal polyhedral model for clinoamphibole. Canadian Mineralogist, 17, 1–10.

Hawthorne, F.C., and Oberti. R. (2007) Amphiboles: crystal chemistry. In Hawthorne, F.C., Oberti, R., Della Ventura, G., Mottana, A. (eds) Amphiboles: Crystal Chemistry, Occurrence, and Health Issues, Reviews in Mineralogy and Geochemistry 67, Min. Soc. Am., Chantilly, Virginia, pp 1–54.

Hawthorne, F.C., Oberti, R., Harlow, G.E., Maresch, W.V., Martin, R.F., Schumacher, J.C., and Welch, M.D. (2012) Nomenclature of the amphibole supergroup. American Mineralogist, 97, 2031–2048. https://doi.org/10.2138/am.2012.4276

Ichiki, M., Baba, K., Toh, H., and Fuji-ta, K. (2009) An overview of electrical conductivity structures of the crust and upper mantle beneath the northwestern Pacific, the Japanese Islands, and continental East Asia. Gondwana Research, 16, 545–562. https:// doi.org/10.1016/j.gr.2009.04.007.

Kasaya, T., Goto, Tn, Mikada, H., Baba, K., Suyehiro, K., and Utada, H. (2005) Resistivity image of the Philippine Sea plate around the 1944 Tonankai earthquake zone deduced by marine and land MT surveys. Earth, Planets and Space, 57, 209–213. https://doi.org/10.1186/BF03351817.

Kittel, C. (2004) Introduction to Solid State Physics. 8nd edition Wiley, New York.

Konzett, J., Sweeney, R.J., Thompson, A.B., and Ulmer, P. (1997) Potassium amphibole stability in the upper mantle: an experimental study in a peralkaline KNCMASH system to 8·5 GPa. Journal of Petrology, 38, 537–568. https://doi.org/10.1093/petroj/38.5.537

Mihailova, B., Della Ventura, G., Waeselmann, N., Xu, W., Schlüter, J., Galdenzi, F., Marcelli, A., Redhammer, G.J., Boiocchi, M., and Oberti, R. (2021) Atomistic insight into lithospheric conductivity revealed by phonon-electron excitations in hydrous iron-bearing silicates. Communications Materials, 2, 1–10. https://doi.org/10.1038/s43246-021-00161-y

Mihailova, B., Della Ventura, G., Waeselmann, N., Bernardini, S., Xu, W., and Marcelli, A (2022) Polarons in rock-forming minerals: physical implications. Condensed Matter 7, 68. https://doi.org/10.3390/condmat7040068

Oberti, R., Boiocchi, M., Zema, M., and Della Ventura, G. (2016) Synthetic potassic-ferro-richterite: 1. composition, crystal structure refinement and HT behavior by in operando single-crystal X-ray diffraction. The Canadian Mineralogist, 54, 1–17. https://doi.org/10.3749/canmin.1500073

Oberti, R., Boiocchi, M., Zema, M., Hawthorne, F.C., Redhammer, G.J., Susta, U., and Della Ventura, G. (2018) The HT behavior of riebeckite: expansivity, deprotonation,

Fe-oxidation and a novel cation disorder scheme. European Journal of Mineralogy, 30, 437–449. https://doi.org/10.1127/ejm/2018/0030-2712.

Redhammer, G.J., and Roth, G. (2002) Crystal structure and Mössbauer spectroscopy of the synthetic amphibole potassic-ferri-ferrorichterite at 298 K and low temperatures (80-110 K). European Journal of Mineralogy, 14, 105–114. https://doi.org/10.1127/0935-1221/2002/0014-0105

Rösche, C., Waeselmann, N., Petrova, N., Malcherek, T., Schlüter, J., and Mihailova, B. (2022) Oxidation processes and thermal stability of actinolite. Physics and Chemistry of Minerals, 49, 47. https://doi.org/10.1007/s00269-022-01223-4.

Susta, U., Della Ventura, G., Hawthorne, F.C., Mihailova, B., and Oberti, R. (2018) The crystal chemistry of riebeckite, ideally $Na_2Fe^{2+}{}_3Fe^{3+}{}_2Si_8O_{22}(OH)_2$: a multi-technique study. Mineralogical Magazine, 82, 837–852. https://doi.org/10.1180/minmag.2017.081.064

Waeselmann, N., Schlüter, J., Malcherek, T., Della Ventura, G., Oberti, R., and Mihailova, B, (2020) Nondestructive determination of the amphibole crystal-chemical formulae by Raman spectroscopy: One step closer. Journal of Raman Spectroscopy, 51, 1530–1548. https://doi.org/10.1002/jrs.5626

Wagner, C., Deloule, E., and Mokhtari, A. (1996) Richterite-bearing peridotites and MARID-type inclusions in lavas from North Eastern Morocco: mineralogy and D/H isotopic studies. Contributions to Mineralogy and Petrology, 124, 406–421. https://doi.org/10.1007/s004100050200

Wilkinson, J.F.G., and Le Maitre, R.W. (1987) Upper mantle amphiboles and micas and TiO_2, K_2O, and P_2O_5 abundances and 100 $Mg/(Mg+Fe^{2+})$ ratios of common basalts and andesites: implications for modal mantle metasomatism and undepleted mantle compositions. Journal of Petrology, 28, 38–73. https://doi.org/10.1093/petrology/28.1.37

Yu, P.Y., and Cardona, M. (2010) Fundamentals of Semiconductors. Springer, New York.

This is the peer-reviewed, final accepted version for American Mineralogist, published by the Mineralogical Society of America.
The published version is subject to change. Cite as Authors (Year) Title. American Mineralogist, in press.
DOI: https://doi.org/10.2138/am-2023-9138. http://www.minsocam.org/

Figures Captions

Figure 1 Sketch of the *C*2/*m* amphibole structure with fully occupied *A* site in two different projections. The dashed rectangle in (b) marks the I-beam of a tetrahedra and octahedra that extends along the **c** axis; the solid ellipse marks the *M*(4) cation connecting three I-beams

Figure 2 Sketch of a polaron formed due to a direct transition across the energy gap E_g in $^{M(1,2,3)}$Fe-bearing amphiboles (a), and of polaron hopping along the TO_4-MO_6 strips (b). The crystallographic-axes compass refers to *C*2/*m*. The dipole moment of the polaron, represented by the thick arrow in (a), is parallel to the I-beam because it arises from an electronic transition between hybridized orbitals of Fe and O within a plane perpendicular to the **c** axis, which couples with a phonon having polarity along the **c** axis (see Mihailova et al. 2021)

Figure 3. *In situ* temperature-dependent polarized $\mathbf{E}_i \parallel \mathbf{c}$ and $\mathbf{E}_i \perp \mathbf{c}$ spectra of potassic-ferro-richterite measured in air (a and b) and in N_2 (c and d). The peaks arising from the MO_6 mode near 198 cm^{-1}, SiO_4-ring mode near 671 cm^{-1}, and the OH stretching mode near 3676 cm^{-1} are shaded with reddish, green and blue, respectively, in the spectra collected at 300 K.

Figure 4. Temperature dependence of the wavenumber of the ring mode near 671 cm^{-1} ($\omega^{\text{ring mode}}_{671\ \text{cm}^{-1}}$) and fractional intensity ($I^{\text{MO}_6}_{n\ 197}$) of the Raman-active MO_6 mode near 197 cm^{-1} in air (a and b) and N_2 (c and d) for potassic-ferro-richterite. Scattering geometries and environment of the *in situ* experiments are given in the plots. The blue symbols represent data collected on cooling.

Figure 5. Temperature dependence of the total Raman scattering arising from the OH-stretching modes $I^{\text{OH stretching}}$ normalized to the total Raman scattering generated by the framework vibrations $I^{\text{framework}}$ from both scattering geometries in air (a and b) and N_2 (d and c) for potassic-ferro-richterite. The blue symbols represent data collected on cooling.

Figure 6. Time-dependent polarized $\mathbf{E}_i \parallel \mathbf{c}$ spectra measured at 300K *in situ* and in N_2 for riebeckite (a) and potassium-ferro-richterite (b) after annealing the samples in N_2 at T" (650K for riebeckite and 525 K for potassium-ferro-richterite, see Table 2) and cooling at 50 K/min. Arrows mark the reappearance of the OH-stretching phonon mode.

Figure. 7 Time dependence of the fractional intensity ($I_{n\,197}^{\mathrm{MO_6}}$) of the Raman-active MO_6 mode near 197 cm^{-1} in the $\mathbf{E}_i \parallel \mathbf{c}$ spectra normalized to the corresponding intensity measured before annealing the sample: $I_{n(t)}^{\mathrm{MO_6}}/I_{n(NA)}^{\mathrm{MO_6}}$ (a). Intensity ratio of the non-RRS peak generated by the ring mode near 660 cm^{-1} and the RRS peak near 580 cm^{-1} $I^{ring\ mode}/(I^{ring\ mode}+I^{RRS})$ (b). All data derived from spectra collected at 300 K in N_2 after annealing the sample at T" for 30 min and cooling down to 300 K with a rate of 50 K/min; NA: non-annealed

Fig.1

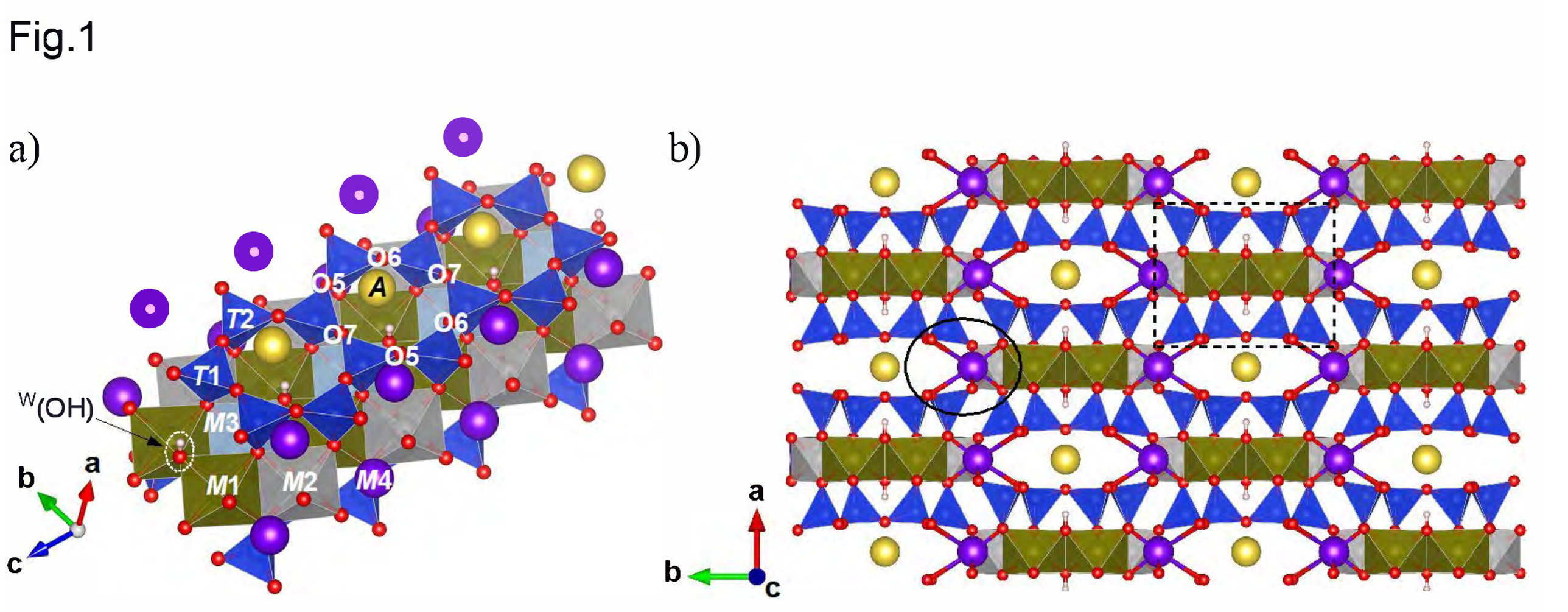

Fig.2

a)

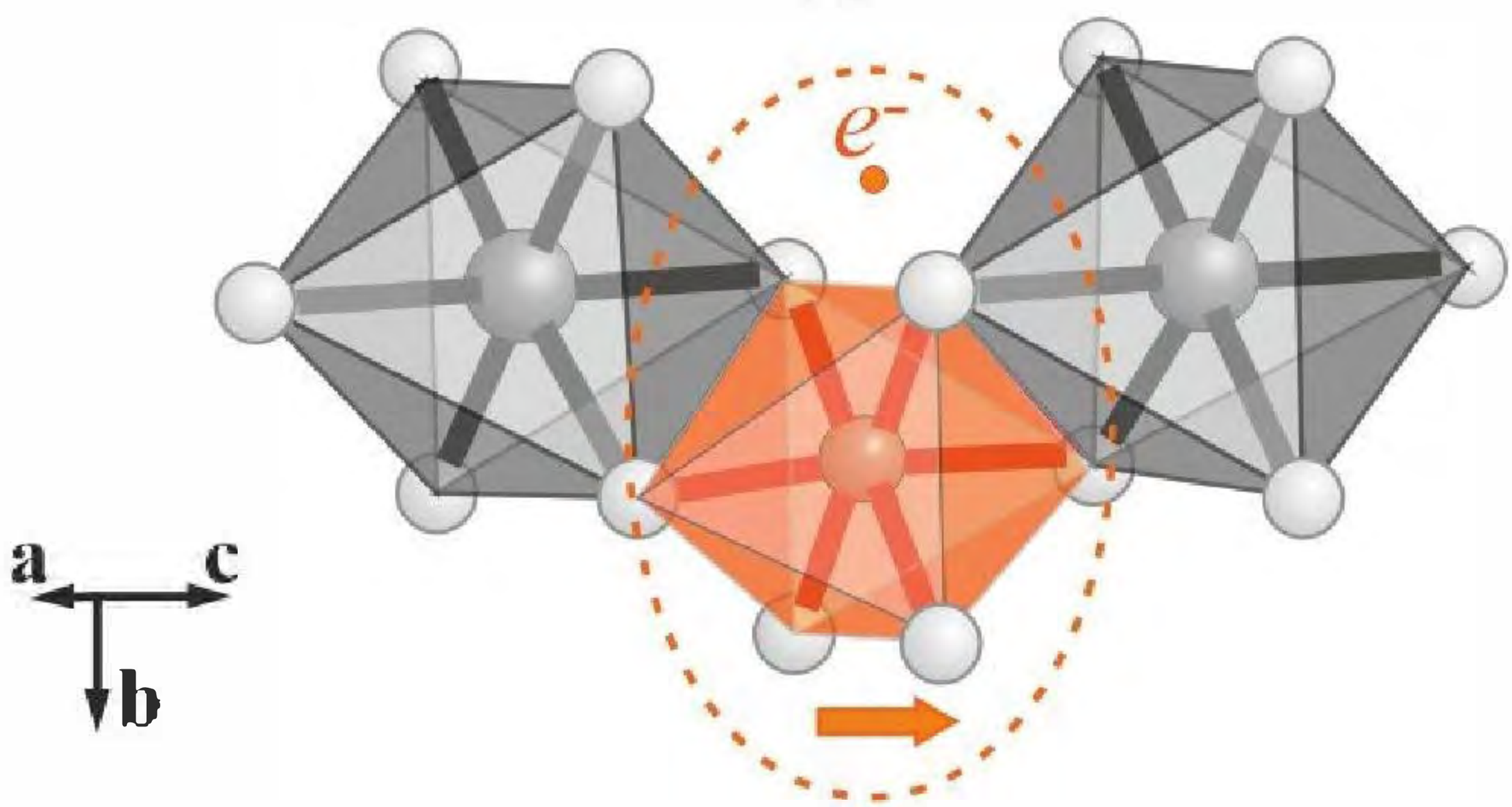

b)

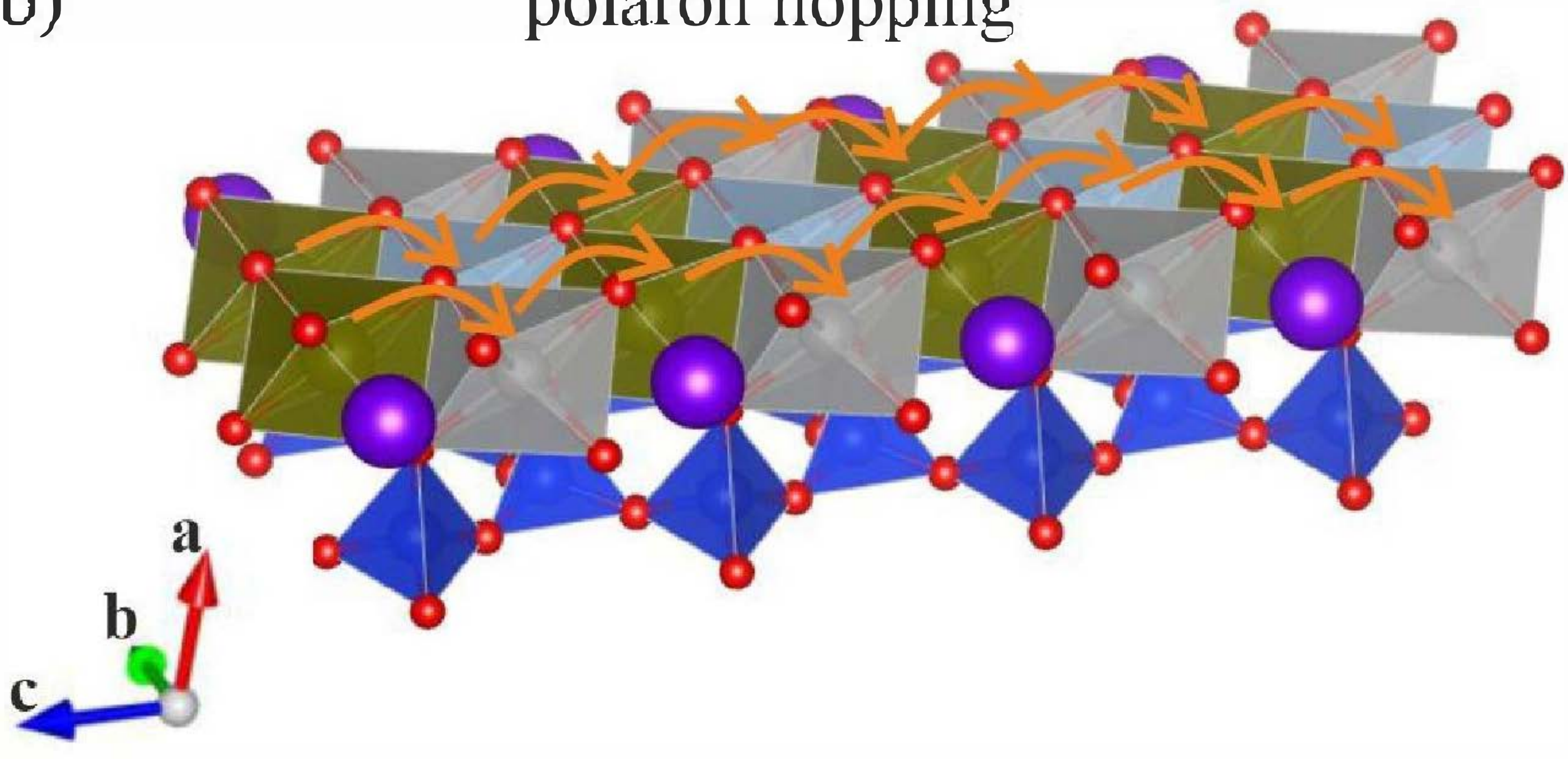

Fig. 3

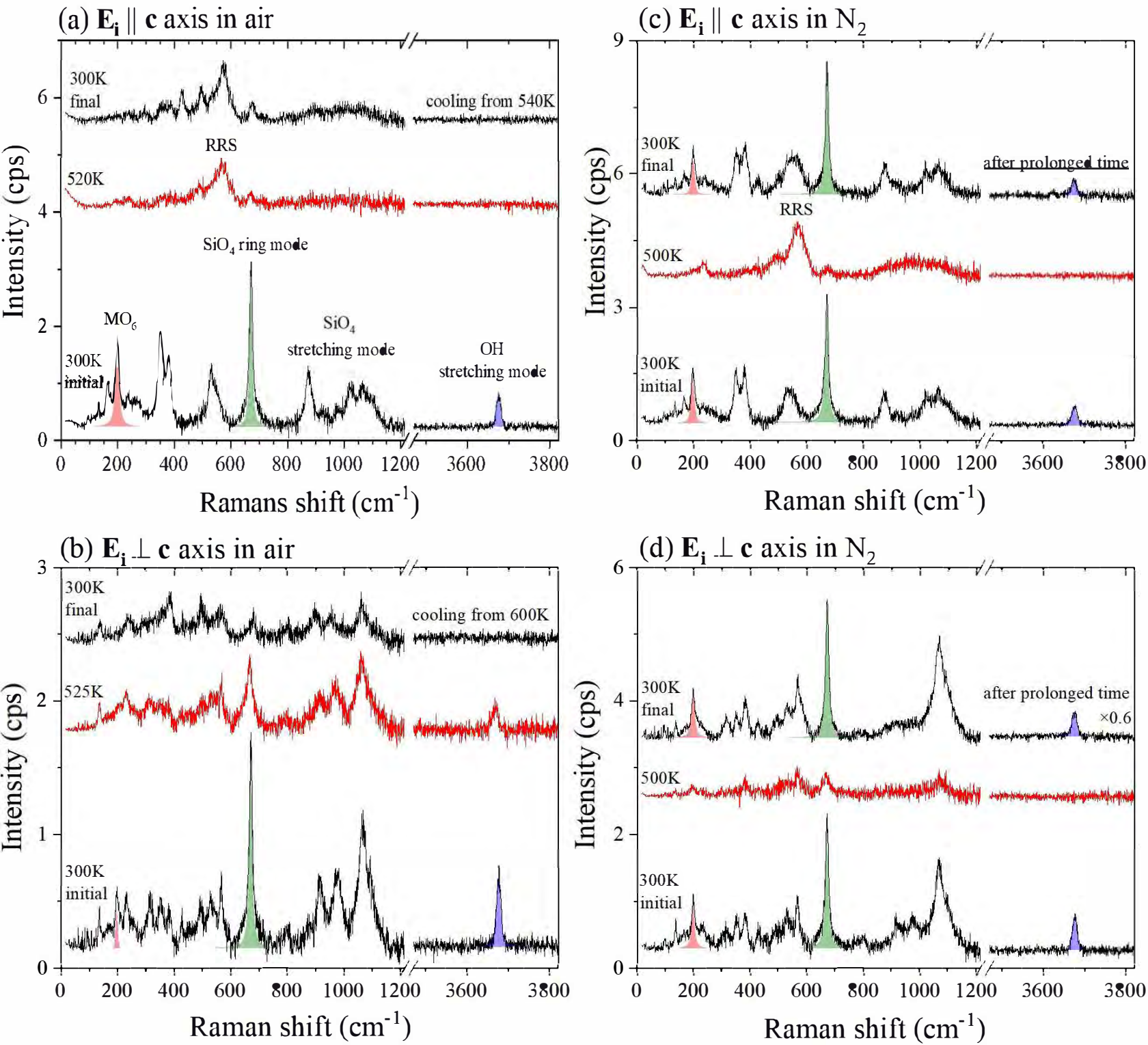
(a) $\mathbf{E_i} \parallel \mathbf{c}$ axis in air
300K final
cooling from 540K
RRS
520K
SiO_4 ring mode
MO_6
SiO_4 stretching mode
OH stretching mode
300K initial
Intensity (cps)
Ramans shift (cm^{-1})
(c) $\mathbf{E_i} \parallel \mathbf{c}$ axis in N_2
300K final
after prolonged time
RRS
500K
300K initial
Intensity (cps)
Raman shift (cm^{-1})
(b) $\mathbf{E_i} \perp \mathbf{c}$ axis in air
300K final
cooling from 600K
525K
300K initial
Intensity (cps)
Raman shift (cm^{-1})
(d) $\mathbf{E_i} \perp \mathbf{c}$ axis in N_2
300K final
after prolonged time
×0.6
500K
300K initial
Intensity (cps)
Raman shift (cm^{-1})

Fig. 4

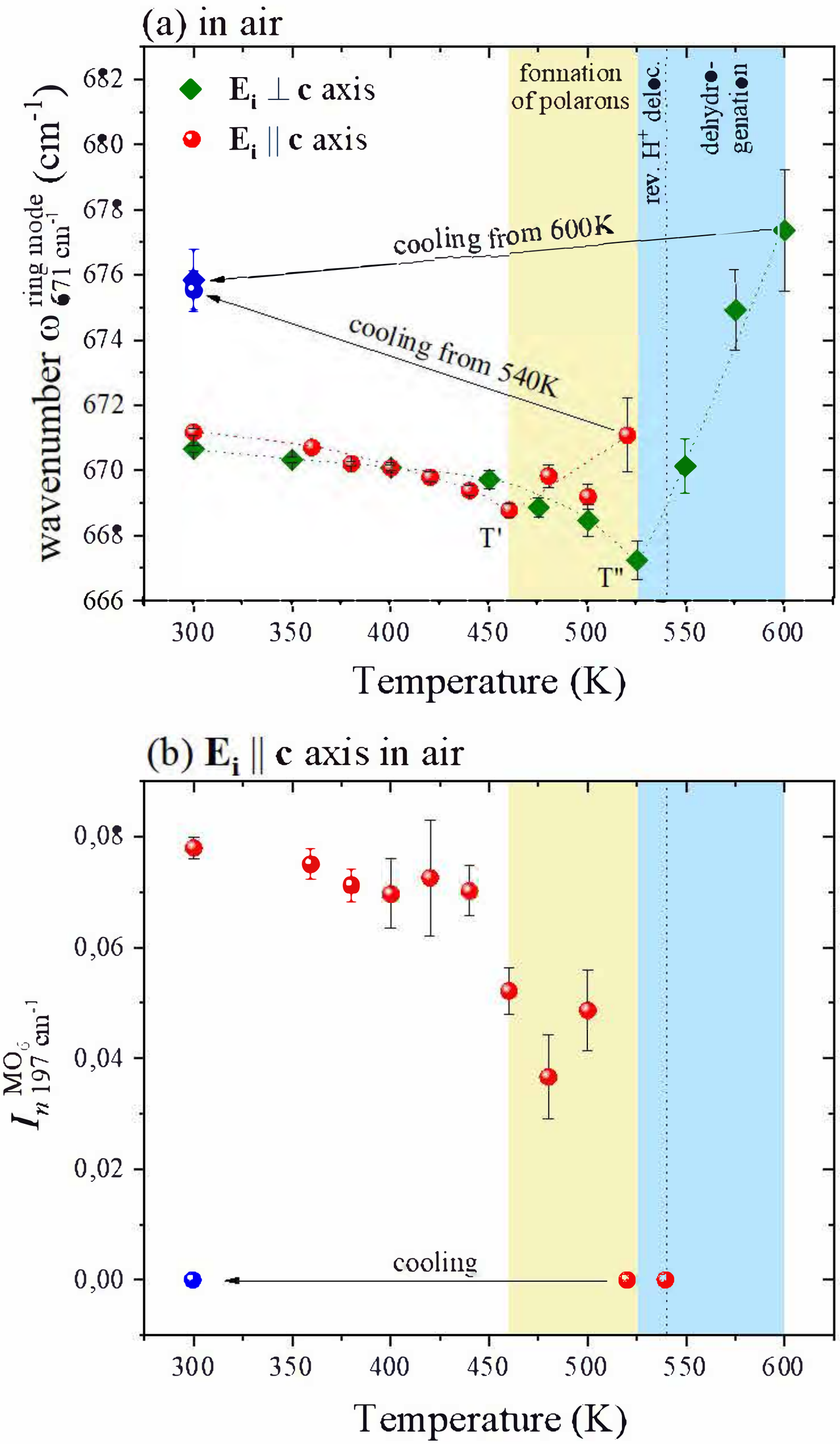
(a) in air
E_i ⊥ c axis
E_i || c axis
formation of polarons
rev. H+ deloc.
dehydro-genation
cooling from 600K
cooling from 540K
T'
T"
wavenumber ω ring mode 671 cm-1
(b) E_i || c axis in air
cooling
Temperature (K)
I_n MO6 197 cm-1

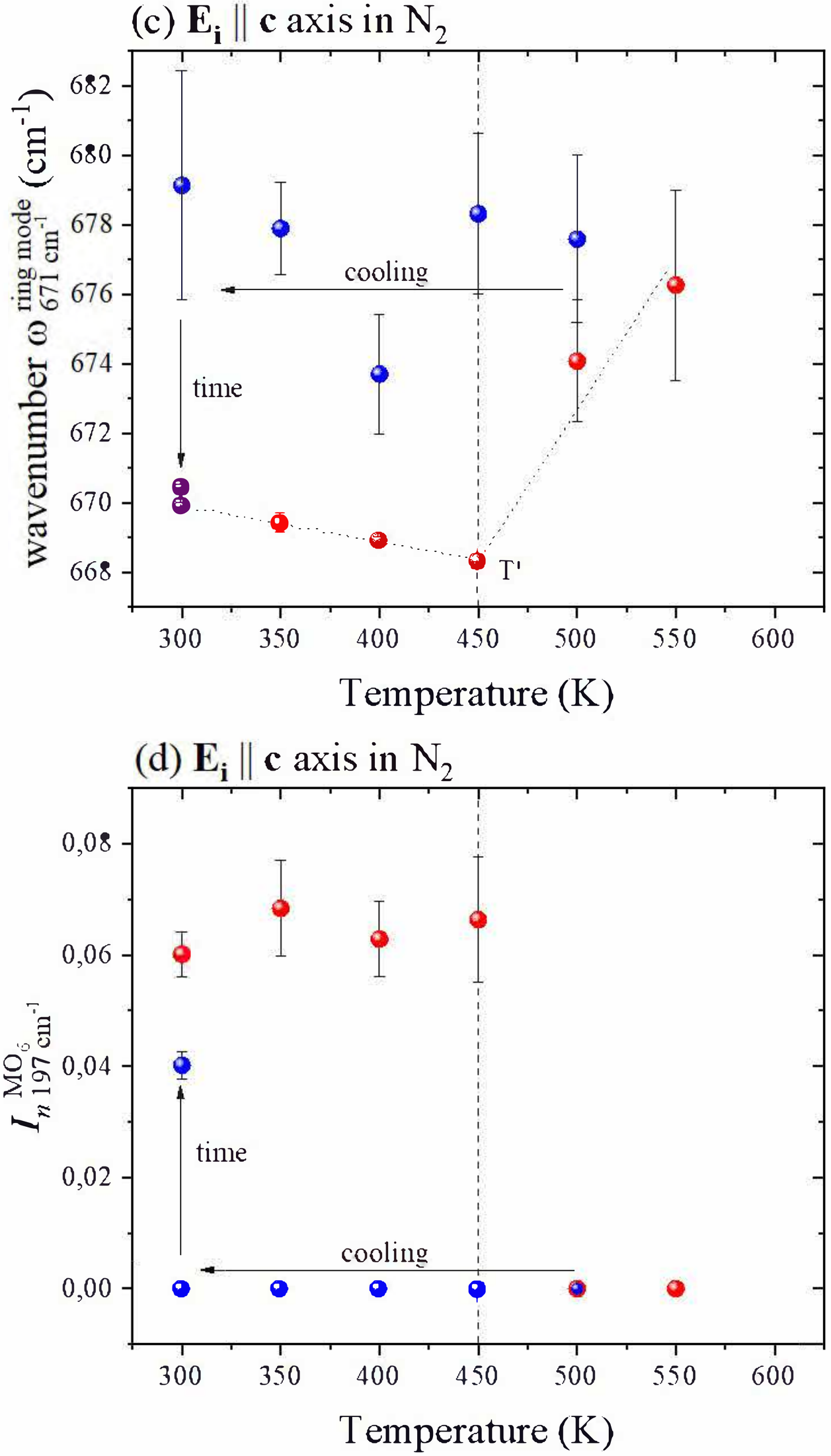
(c) E_i || c axis in N2
cooling
time
T'
wavenumber ω ring mode 671 cm-1
(d) E_i || c axis in N2
time
cooling
Temperature (K)
I_n MO6 197 cm-1

Fig.5

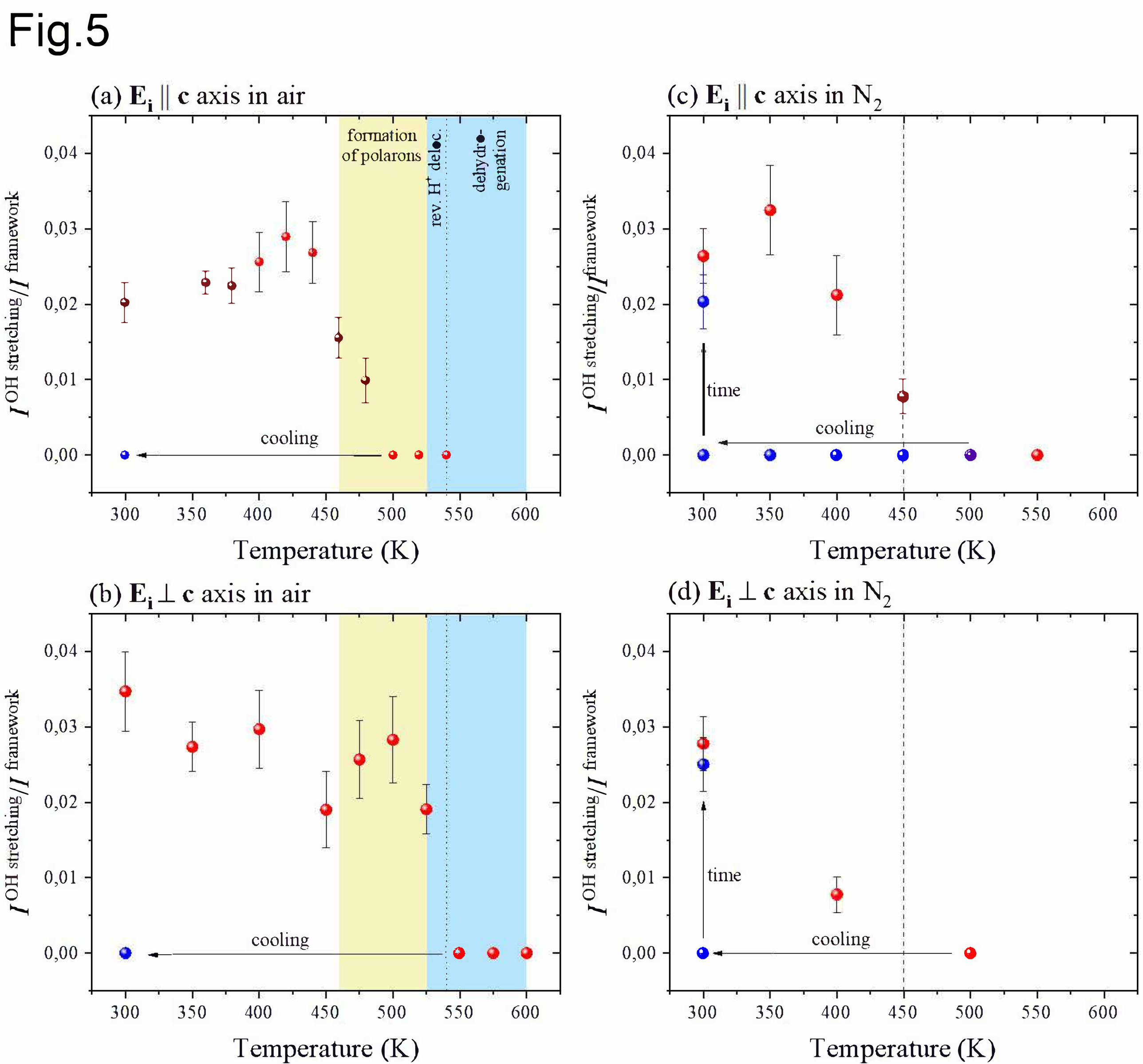
(a) E_i || c axis in air
(b) E_i ⊥ c axis in air
(c) E_i || c axis in N_2
(d) E_i ⊥ c axis in N_2
formation of polarons
rev. H^+ delc.
dehydr- genation
cooling
time
$I^{OH\ stretching}/I^{framework}$
0,00
0,01
0,02
0,03
0,04
300
350
400
450
500
550
600
Temperature (K)

Fig. 6

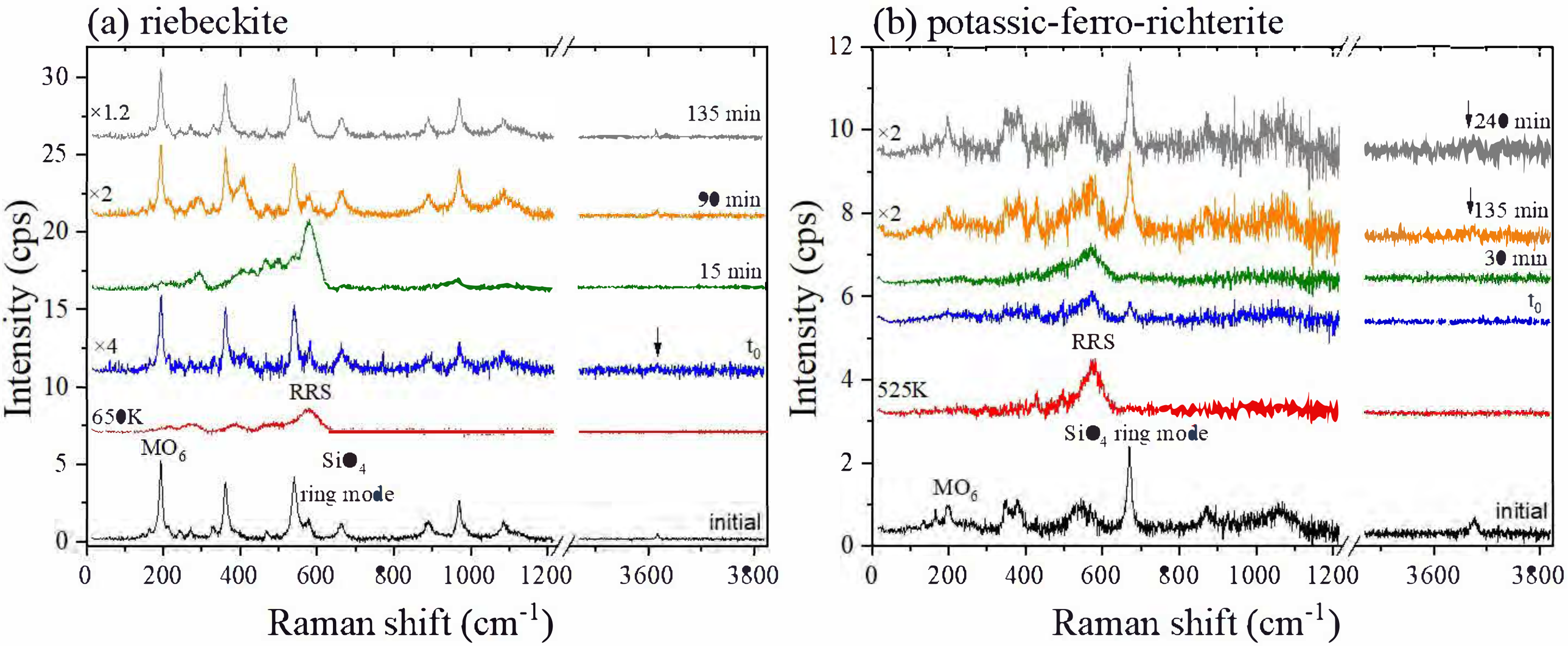
(a) riebeckite
(b) potassic-ferro-richterite
Intensity (cps)
Raman shift (cm-1)
×1.2
×2
×4
135 min
90 min
15 min
t0
RRS
650K
MO6
SiO4
ring mode
initial
525K
240 min
30 min

Fig. 7

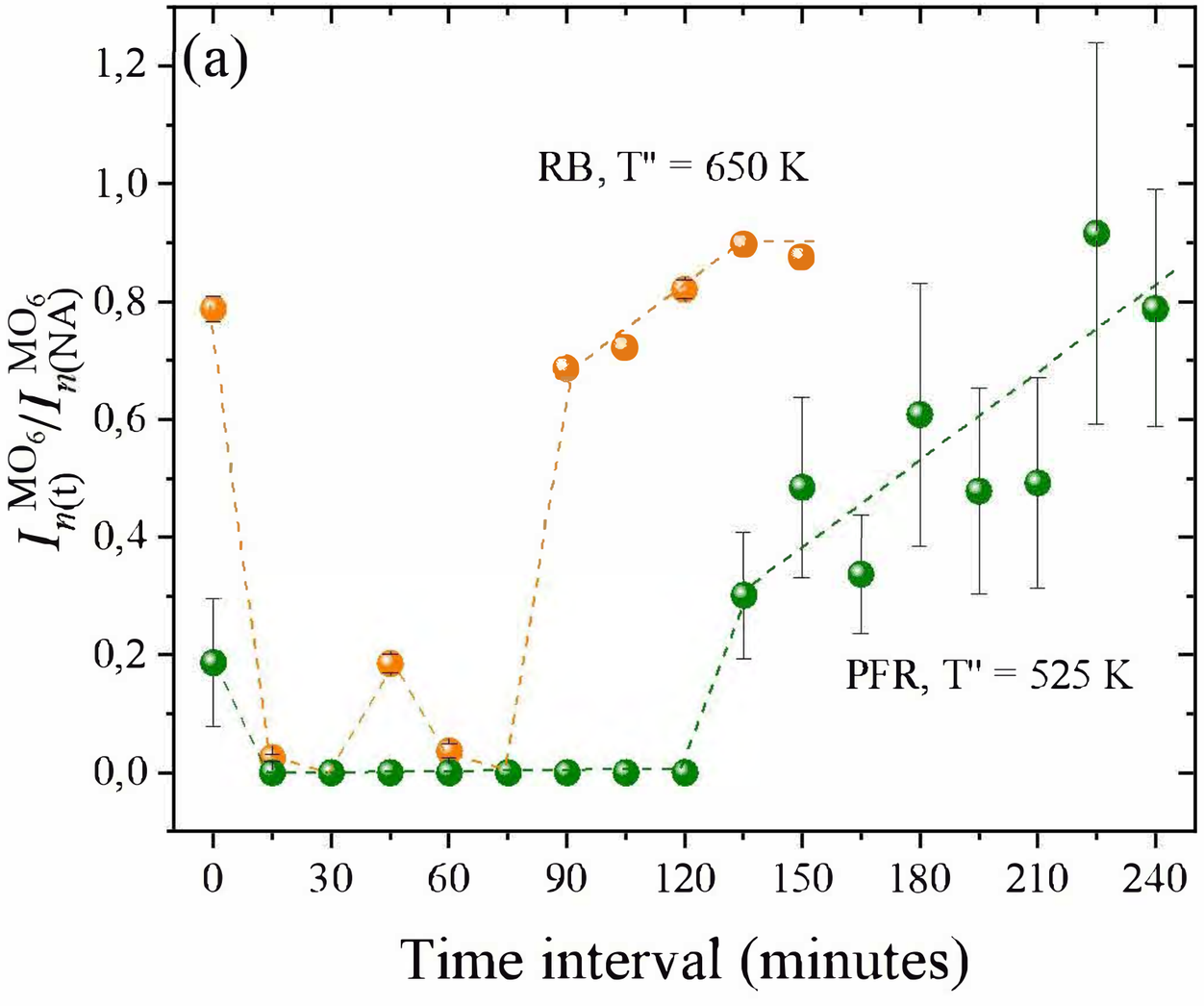
(a)
RB, T" = 650 K
PFR, T" = 525 K
$I^{MO_6}_{n(t)}/I^{MO_6}_{n(NA)}$
Time interval (minutes)

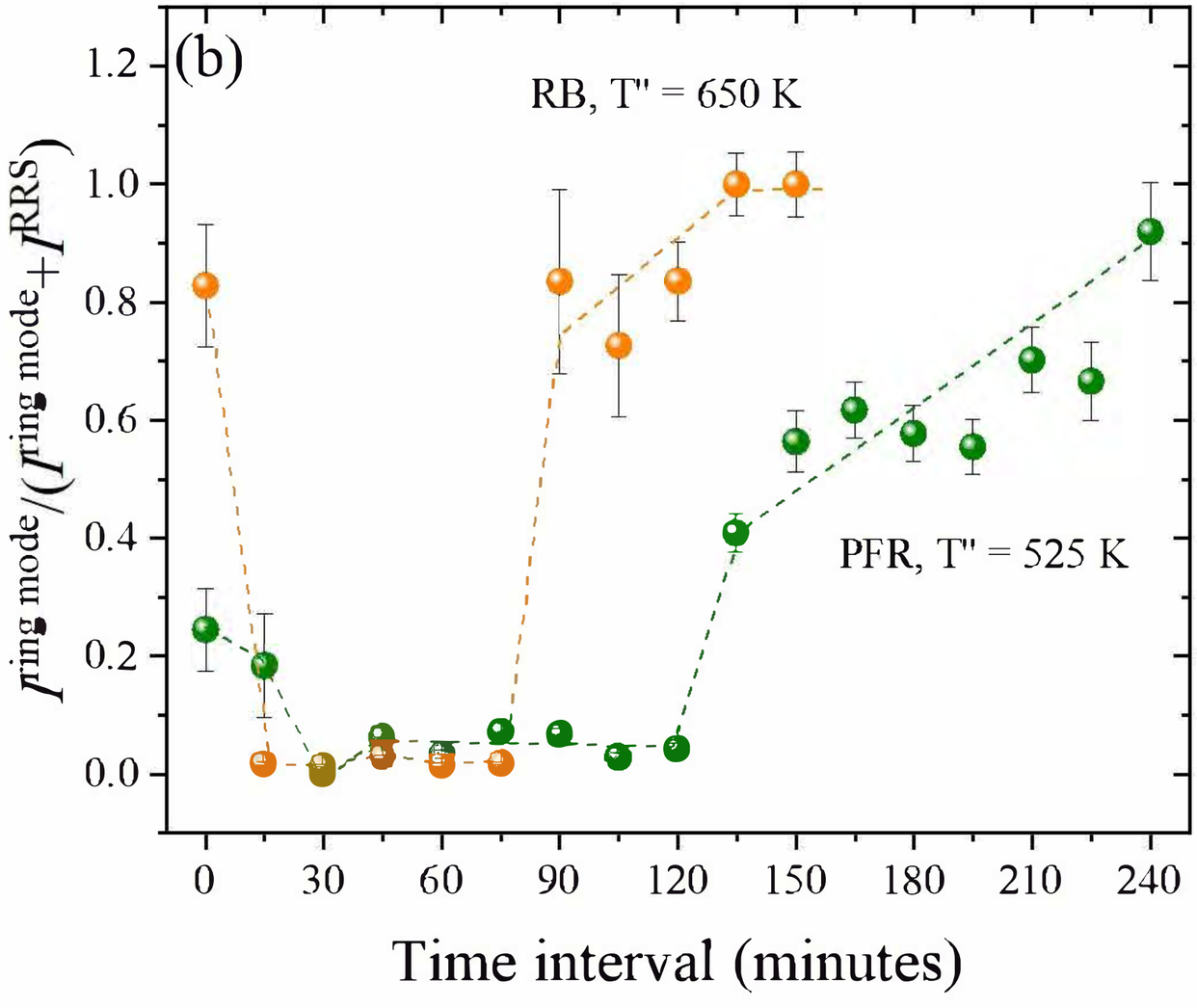
(b)
RB, T" = 650 K
PFR, T" = 525 K
$I^{ring\ mode}/(I^{ring\ mode}+I^{RRS})$
Time interval (minutes)

Table 1. Summary of experimental runs for the *in situ* temperature-dependent experiments on PFR. Temperatures are given in Kelvins and in bold (on heating) or in italic (on cooling).

scattering geometry	atmosphere	
	air	N_2
$\mathbf{E_i}$ ‖ **c** axis	**300**, **360**, **380**, **400**, **420**, *300*, **440**, *300*, **460**, *300*, **480**, *300*, **500**, *300*, **520**, *300*, **540**, *300*, **600**, *300*	**300**, **350**, **400**, **450**, **500**, **550**, *500*, *450*, *400*, *350*, *300*, *300* (after t >120min)
$\mathbf{E_i} \perp$ **c** axis	**300**, **350**, **400**, **450**, **475**, **500**, **525**, **550**, *300*, **575**, *300*, **600**, *300*	**300**, **400**, **500**, *300*, *300* (after ~120 min)

Table 2. Summary of characteristic temperatures derived from Raman-scattering data and the calculated $|\delta \mathbf{U}|$ for riebeckite (RB), potassic-ferro-richterite (PFR), and grunerite (GR). T': onset of formation of polarons. T'': complete generation of mobile polarons and delocalization of H^+. T''-T' and consequently $|\delta \mathbf{U}|$ are indicative of the average magnitude of polaronic dipoles. Data from: [a]Bernardini et al. 2023; [b]Mihailova et al. 2021, 2022.

Amphibole species	Nominal formulae	T' (K)	T'' (K)	T''-T' (K)	$\lvert\delta \mathbf{U}\rvert$ (eV)
PFR (occupied *A*-site)	$^{A}K^{B}(CaNa)^{C}Fe^{2+}{}_{5}{}^{T}Si_{8}O_{22}(OH)_{2}$	460	525	~65	~0.005
RB (empty *A*-site)[a]	$^{A}\square^{B}Na_{2}{}^{C}(Fe^{2+}{}_{3}Fe^{3+}{}_{2})^{T}Si_{8}O_{22}(OH)_{2}$	500	650	~150	~0.013
GR (empty *A*-site)[b]	$^{A}\square^{B}Fe_{2}{}^{C}Fe^{2+}{}_{5}{}^{T}Si_{8}O_{22}(OH)_{2}$	700	850	~150	~0.013